Journal of Materials Chemistry A

Accepted Manuscript

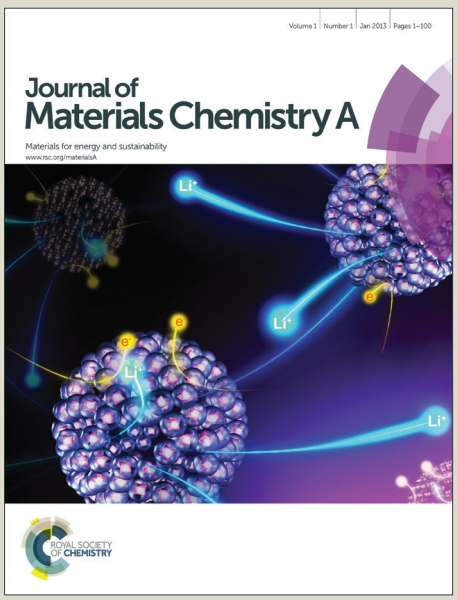

ROYAL SOCIETY OF CHEMISTRY

www.rsc.org/materialsA

Cite this: DOI: 10.1039/c0xx00000x

www.rsc.org/xxxxxx

ARTICLE TYPE

Three Dimensional Mn_3O_4 Network Supported on Nitrogenated Graphene Electrocatalyst for Efficient Oxygen Reduction Reaction in Alkaline Media

Santosh Kumar Bikkarolla[1], Fengjiao Yu[2], Wuzong Zhou[2], Paul Joseph[3], Peter Cumpson[4], and Pagona Papakonstantinou[1*]

Received (in XXX, XXX) Xth XXXXXXXXX 20XX, Accepted Xth XXXXXXXXX 20XX
DOI: 10.1039/b000000x

Developing low cost oxygen reduction catalysts that perform with high efficiency is highly desirable for the commercial success of environmentally friendly energy conversion devices such as fuel cells and metal-air batteries. In this work a three dimensional, 3D, self-assembled Mn_3O_4 hierarchical network has been grown on nitrogen doped reduced graphene oxide (NrGO), by a facile and controllable electrodeposition process and its electrocatalytic performance for oxygen reduction reaction (ORR) has been assessed. The directly electrodeposited MnO_x on the glassy carbon electrode (GCE) exhibits little electrocatalytic activity, whereas the integrated Mn_3O_4/NrGO catalyst is more ORR active than the NrGO. The resulting electrode architecture exhibits an "apparent" four-electron oxygen reduction pathway involving a dual site reduction mechanism due to the synergetic effect between Mn_3O_4 and NrGO. The 3D Mn_3O_4/NrGO hierarchical architecture exhibits improved durability and methanol tolerance, far exceeding the commercial Pt/C. The enhanced ORR performance of the room temperature electrodeposited Mn_3O_4 nanoflakes network integrated with NrGO reported here, offers a new pathway for designing advanced catalysts for energy conversion and storage.

Introduction

The development of catalytic materials for the oxygen reduction reaction (ORR) is one of the major challenges in electrochemical energy conversion and storage technologies such as fuel cells and metal−air batteries.[1, 2] The ORR reaction at the cathode proceeds through a multistep electron transfer, leading to sluggish kinetics and a large overpotential. This large overpotential is related to the difficulty in O_2 adsorption on electrode surface and O=O bond cleavage. An effective electrocatalyst such as platinum is needed in order to reduce the overpotential and expedite the reaction, through a single step four electron transfer process.[2] However, the high use of platinum needed for achieving efficient ORR and its high cost due to the platinum's rarity is one of the most important factors hindering the applicability of these devices to broad commercialization. An added reason is that Pt catalysts are vulnerable to poisoning by adsorption of the reaction intermediates and to the fuel crossover effect, which limits substantially their performance. To date, there have been notable improvements towards developing highly active and durable alternatives based on low cost earth abundant metal catalysts, such as the first-row transition metal oxides,[3-7] spinels[8-11] and perovskites.[12-15] However, most non-precious metal catalysts developed so far still underperform the Pt benchmark.

Among the non-precious metal alternatives, manganese oxides have received intensive attention because of their high element abundance, low cost and toxicity and appreciable activity, when integrated with a conductive based support material such as graphene, carbon nanotubes or ketjen black.[16-27] The ORR activity is dependent on the particle size and morphology as well as on phase of the Mn oxide in the following order: MnOOH > Mn_2O_3 > Mn_3O_4 > Mn_5O_8.[28] Manganese oxides with higher valence show better catalytic activity towards ORR and the surface Mn valance can be tuned with simple electrochemical cycling or heat treatment.[6, 7, 28] Nevertheless, irrespective of their phase, manganese oxides, when used on their own, show mediocre electrocatalytic activity due to their low conductivity. Strategies to enhance their conductivity and hence facilitate electron transport for ORR include doping with cations,[24, 29, 30] coating with metals and coupling with conductive nanostructures.[16-27] Currently, intricate synthesis routes and medium performance disfavour their use as inexpensive and robust ORR catalysts in technological systems. Manganese oxides directly electrodeposited on conductive electrodes represent an attractive option, however deposition routes on standard electrodes such as GCE resulted in oxides of comparatively low catalytic activity in the as deposited state requiring high temperature annealing to create active crystalline phase.[31, 32]

Bearing in mind that nitrogenated reduced graphene oxide is both ORR active and highly conductive, it is intuitive to use NrGO as a support electrode for the electrochemical deposition of manganese oxides and study their synergetic coupling effect. The ORR activity in nitrogen doped graphene has been rationalized using density functional calculations, where it was found that nitrogen doping alters the local spin or charge density thus promoting oxygen adsorption.[33, 34] So far only a few studies have

explored Mn_3O_4/N-doped graphene hybrids as ORR catalysts, with the Mn_3O_4 in the form of various shapes (spheres, cubes and ellipsoids)[16, 18, 22, 23, 25] or Mn_3O_4 nanoparticles encapsulated in nitrogen doped graphene.[19] However their synthesis is based on solvothermal or reflux methods requiring low or high temperature steps to induce a highly crystalline Mn_3O_4 phase for providing ORR catalytic sites. The ORR performance of Mn_3O_4 catalysts in the form of nanoflakes, integrated on NrGO has never been investigated before.

Herein, direct growth of a three dimensional poorly crystalline Mn_3O_4 network on conductive NrGO was achieved by simple electrodeposition at room temperature. The integrated Mn_3O_4/NrGO structure displays high electrocatalytic activity with an apparent four-electron ORR in alkaline solution. The improved performance of the Mn_3O_4/NrGO hierarchical nanostructure is attributed to the following factors: (i) the direct growth of Mn_3O_4 network on the underlying conductive NrGO provides strong coupling between the two catalysts, which affords coupled reactions leading to improved performance. In addition the strong coupling also reduces the interfacial resistance and improves electron transport; (ii) the highly porous Mn_3O_4 network with moderate long range order affords a high density of surface defects, which potentially act as active sites for oxygen adsorption, contributing to the ORR activity. Our study is distinctively different from previous ones that examine Mn_3O_4/N-doped graphene hybrids based on temperature dependent solvothermal or reflux methods. In contrast to previous studies that concentrate on well crystallized Mn_3O_4, we have found that due to the absence of any high temperature step the Mn_3O_4 nanoflakes are not highly crystalline but possess a moderate long range order, which contributes to the efficient ORR activity by providing ample defect sites for oxygen absorption.

Experimental section

Chemicals

Graphite powder (particle size < 20 μm) purchased from Alfa Asar. Sodium nitrate ($NaNO_3$), potassium permanganate ($KMnO_4$), ammonia hydroxide (30 wt% in H_2O), hydrazine solution (35 wt% in H_2O), N N-dimethylformamide (DMF), manganese acetate ($Mn(CH_3COO)_2$), sodium sulphate (Na_2SO_4), alumina (particle size 0.05 μm) are purchased from Sigma Aldrich. All solutions used in electrochemical experiments were freshly prepared with Millipore water of resistivity 15 MΩ.

Synthesis of graphene oxide

Graphene oxide was produced by using modified Hummer's method.[62, 63] Graphite powder of particle size 20 μm was used as starting material. 2.5 g of graphite, 2 g of $NaNO_3$ and 85 ml of H_2SO_4 were mixed together in a 250 ml round bottom flask in an ice bath to form a homogenous mixture. Solution of 11.25 g of $KMnO_4$ in distilled water was gradually added to the solution. After 2 hrs the solution was removed from ice bath and stirred at room temperature for five days. The brown color slurry was added to 500 ml of 5 wt% H_2SO_4 and gradually 10 ml of H_2O_2 (30 wt% in H_2O) was added to the mixture and stirred for 24 hrs. The mixture was centrifuged and residue was further purified by dispersing in 500 ml of aqueous solution of 3 wt% H_2SO_4 and 0.5 wt% H_2O_2. After 24 hrs of stirring the supernatant was removed. The process was repeated for five times. The solid product obtained after rigorous cleaning process was rinsed with copious amount of water and dried in oven.

Synthesis of nitrogen doped graphene

GO was exfoliated in water by ultrasonication for 2 hrs. GO dispersion is centrifuged at 1000 rpm for 5 min to remove any thicker graphite oxide and the supernatant is centrifuged at 3000 rpm for 30 min. The obtained graphene oxide pellet is dried in oven at 60°C for 48 hrs. NrGO is synthesized through hydrothermal reaction of graphene oxide with ammonia and hydrazine.[36] In a typical experiment as synthesized graphite oxide is suspended in water to give a concentration of 1 mg/ml followed by sonication of 2 hrs. 70 ml of above solution pH is adjusted to 10 by ammonia hydroxide and 1 ml of hydrazine (35 wt% in H_2O) is added to the solution and stirred for 15 min. The solution was transferred to 100 ml teflon lined vessel to carry out the hydrothermal reaction at 160°C for three hours. The resultant product is cleaned with plenty of DI water and collected by centrifugation at 3000 rpm for 45 min. The pellet is dried under vacuum at 60°C for 48 hrs.

Electrodeposition of Mn_3O_4 nanoflakes on NrGO

5 mg of NrGO is dispersed in 1 ml of DMF with 50 μl of nafion through one hour sonication to form homogenous ink. 6 μl (30 μg) of NrGO suspension is spread on 3 mm GCE and dried under infrared lamp, which results in a final loading of 0.425 mg/cm^2. First NrGO ORR performance is measured in O_2 saturated 0.1 M KOH solution and then Mn_3O_4 nanoflakes were electrodeposited on NrGO. The fabrication process is shown in Figure 1. The electrochemical deposition is carried out in 0.1 M Na_2SO_4 + 0.05 M $Mn(CH_3COO)_2$ in the potential range 0 to -1.5 V(Vs. Ag/AgCl) at a scan rate of 50 mV/sec under two consecutive scans. To determine the density of the Mn_3O_4/NrGO, NrGO is drop dried on both sides of a large glassy carbon substrate (2.5 cm x 2.5 cm) and weighed before and after electrodeposition by micro balance and the density of the Mn_3O_4/NrGO is estimated to be 0.45 mg/cm^2. Mn_3O_4 nanoflakes were electrodeposited on GCE for 2-10 CVs and 1μlone micro liter of nafion (0.25% in isopropanol) is drop dried on Mn_3O_4/GCE to hold the material during electrochemical measurements. In the case of Pt/C, 5 mg of Pt/C (20 wt% Pt on Vulcan XC-72) is dispersed in 1 ml of DMF and 50 μl of nafion by 1 hrs sonication. 4 μl of Pt/C is drop dried on 3 mm GCE and dried under infrared lamp, which results in catalyst loading of 0.28 mg/cm^2.

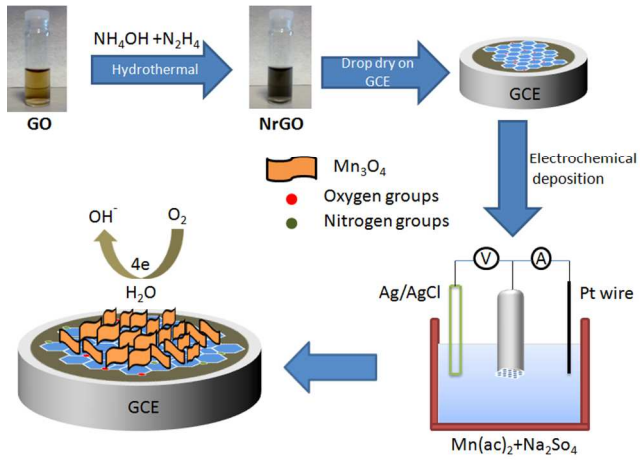

Figure 1 Schematic representation of the steps used in the synthesis of Mn_3O_4/NrGO.

Structural characterization

X-ray photo emission spectroscopy is carried on a Kratos Axis Nova XPS equipped with A1 Kα (hv=1486.6 eV) X-ray source at NEXUS laboratory. X-ray diffraction (XRD) analysis is performed on a Bruker D8-discover diffractometer fitted with global mirror (Cu Kα radiation source λ=1.540 Å). Scanning electron microscopy images were obtained on FEI quanta 200 3D at 20 kV accelerating voltage. High resolution transmission electron microscopy (HRTEM) images were obtained on Jeol JEM 2011. Raman spectroscopy was done with ISA Lab ram equipped with 633 nm laser.

For XPS measurement NrGO dispersed in DMF and nafion is drop dried on GCE substrate of dimension 2.5 cm x 2.5 cm and Mn_3O_4 nanoflakes were electrodeposited from 0.1 M Na_2SO_4 + 0.05 M $Mn(CH_3COO)_2$ solution. For XRD measurement the material is scrapped off from GCE substrate and redispersed in 70% ethanol and drop dried on Si substrate. The TEM samples were prepared by carefully removing the material from the GCE electrode using ultrasonication in isopropanol and coating the TEM grids with few microliters of the solution. SEM imaging and Raman spectroscopy of Mn_3O_4/NrGO were carried out on GCE substrate itself.

Electrochemical measurements

A rotating disk electrode with a glassy carbon disk of 3 mm diameter was used in this study. Prior to surface modification the electrode is polished with alumina powder of particle size 0.05 µm and then cleaned by sonication in water for 2 min. A Pt wire and Ag/AgCl electrode were used as collector and reference electrodes. The electrolyte is 0.1 M KOH is freshly prepared and experiments were carried out at room temperature. The electrolyte is saturated with O_2/Ar by bubbling O_2/Ar for 15 min. A flow of O_2/Ar is maintained over the electrolyte during the measurements. Cyclic voltammograms were collected at a scan rate 0.1 v/sec after at preconditioning the electrode through 25 CVs. RDE measurements were collected at a scan rate of 10 mV/sec and the base line in Ar saturated electrolyte is subtracted.

The electron transfer numbers are calculated with Koutecky-Levich equation as given below.

$$\frac{1}{J} = \frac{1}{J_L} + \frac{1}{J_K} = \frac{1}{nFkC_0} + \frac{1}{0.62nFD^{\frac{2}{3}}\vartheta^{-\frac{1}{6}}C_0\omega^{\frac{1}{2}}} \qquad (1)$$

Where J is the measured current density, J_K and J_L are kinetic and limiting diffusion current densities. n is the electron transfer number in the ORR process. F is the Faraday constant (96500 C/mol), C_0 is the bulk concentration of O_2 (1.2×10^{-6} mol/cm^3), D is the diffusion constant of O_2 in 0.1 M KOH (1.9×10^{-5} cm^2/sec), ν is the kinematic viscosity of the electrolyte (0.01 cm^2/sec) and ω is the angular frequency of the disk (=2πN, N is the linear frequency) and k is electron transfer rate constant.

Results and Discussion

The synthesis of Mn_3O_4/NrGO nanostructure is illustrated in Figure 1. First NrGO was produced through hydrothermal treatment of graphene oxide in the presence of ammonia and hydrazine. Mn_3O_4 nanoflakes were electrodeposited onto a pre-coated NrGO glassy carbon electrode through a voltage cycling protocol in the voltage range 0 to -1.5 V vs Ag/AgCl in a solution of manganese acetate and sodium sulphate.[35]

The morphological and microstructural changes were investigated by scanning electron microscopy (SEM) and transmission electron microscopy (TEM). It can be seen from the SEM images of Figures 2a and 2b that the nitrogenated reduced graphene oxide demonstrated a 3D flame like appearance possessing an interconnected three-dimensional porous network. Low magnification TEM images exhibited a wrinkled morphology, which is characteristic of graphene produced via harsh oxidative and reduction treatments and is indicative of defective structure.[35] The selected area electron diffraction (SAED) yielded a ring-shaped pattern indicative of random overlay of NrGO layers. Each set of layers provides a well-defined set of diffraction spots, which make regular hexagons (e.g., the one inserted in Figure 2c), with different rotational angles. The edge-on views at a high magnification confirm a crystalline interior and are composed of a stack of 5-7 layers. The average interlayer distance is 0.37 nm. Compared to the graphite interspacing of 0.34 nm, this enlarged interspacing indicates a moderate oxidation level present in the NrGO, which is in agreement with the XPS results, presented later.

Shown in Figure 3a and 3b are low and high magnification SEM images of the hierarchical structure of the Mn_3O_4/NrGO nanostructure. The Mn_3O_4 nanoflakes are interconnected with each other, forming a highly porous surface morphology. The formation of the nanoflakes is initiated by strong electrostatic interactions between the oxygen functional groups of the NrGO and the Mn cations, providing the nucleation sites. After only two deposition cycles, nanoflakes appeared and were assembled to form a hierarchical structure. Figure 3c and 3d show TEM and high resolution TEM (HRTEM) images of Mn_3O_4 nanoflakes on NrGO. These TEM samples were prepared by carefully removing the material from the GCE, followed by ultrasonication in isopropanol and coating the TEM grids (lacey carbon coated copper grids) with few drops. From Figure 3c it can be seen that the Mn_3O_4 nanoflakes are firmly anchored on NrGO even after

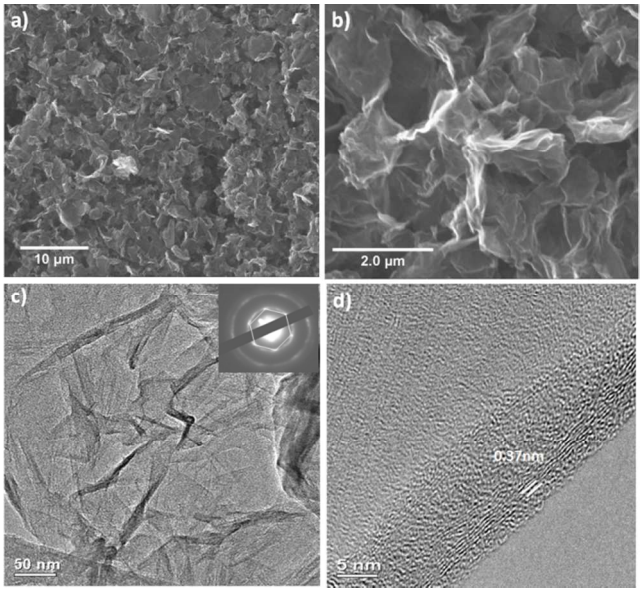

Figure 2. (a-b) SEM images of NrGO. (c) TEM image of NRGO sheet. Inset: a SAED pattern. (d) HRTEM at the folded edge of NrGO.

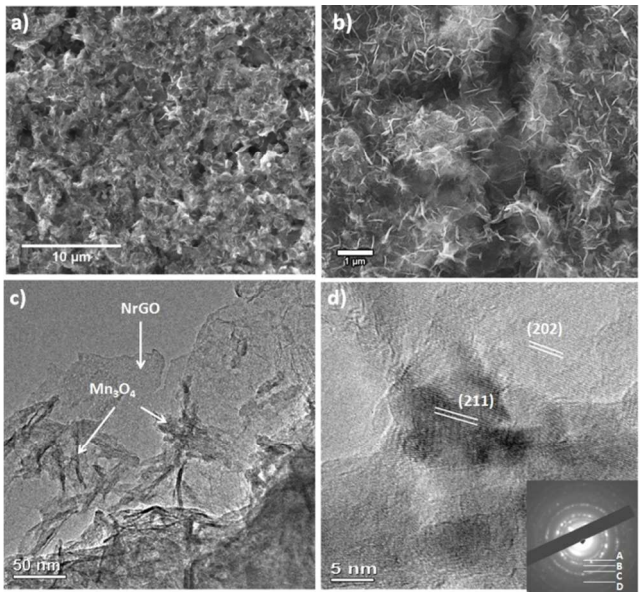

Figure 3. (a-b) Low and high magnification SEM images of Mn_3O_4/NrGO/GCE. (c) TEM image of Mn_3O_4 nanoflakes on NrGO. (d) HRTEM image of Mn_3O_4/NrGO.The inset is a SAED pattern obtained from this nanoflake, showing a polycrystalline nature. The marked diffraction circles correspond to A: (200), B: (211), C: (204), D: (116) of Mn_3O_4.

ultrasonic dispersion, indicating a strong linkage between NrGO sheets and Mn_3O_4 nanoflakes. The arrows mark the edges of Mn_3O_4 nanoflakes on NrGO. The high-resolution TEM image of Mn_3O_4 nanoflakes in Figure 3d (and S8) shows the presence of polycrystalline subunits with various grain boundaries and growth directions. Crystal lattice fringes with d-spacing of 0.25nm and 0.24 nm can be assigned to the (211) and (202) planes respectively of Hausmannite Mn_3O_4. The selected area diffraction (SAED) pattern taken from a Mn_3O_4 nanoflake also confirms the polycrystalline nature. The marked diffraction circles correspond to (200), (211), (204) and (116) planes of Mn_3O_4.

The polycrystalline phase of the hierarchical structure was confirmed by XRD (Figure 4a). The XRD pattern of NrGO shows two distinctive peaks at 24.5° and 43.0° corresponding to the (002) and (100) reflections of graphitic carbon.[36] The average interlayer distance was calculated 3.62 Å, similar to that obtained from HRTEM measurements. The pattern of the hierarchical structure, in addition to characteristic peaks associated with NrGO and nafion, displays weak and significantly broadened diffraction peaks at 32.6°, 36.2° and 38.5° revealing poor crystallinity. The peaks are indexed to (103), (211), and (004) crystal planes of the tetragonal Hausmannite Mn_3O_4 structure (a=5.65 Å and c=9.44 Å, JCPD card no: 80-0382). The results reveal that room temperature electrochemical synthesis process leads to a poorly crystalline form of manganese oxide with a moderate degree of long range order, which may offer more active sites for ORR.

Interestingly, the I_D/I_G intensity ratio increases from 1.05 for GO to 1.4 for NrGO and Mn_3O_4/NrGO as shown in Figure 4b. Naturally, one would expect a decrease in the I_D/I_G ratio upon hydrothermal treatment of GO since the disorder associated with the semi-amorphous graphene oxide diminishes. It is well documented that the ratio of the D and G peak is a measure of the size of sp^2 ring clusters in a network of sp^2 and sp^3 carbon.

Therefore the observed increase in I_D/I_G is indicative of a decrease in the size of sp^2 domains upon reduction. The origin of this reduction is not well understood, however various suggestions have been proposed.[37, 38] One hypothesis is that the hydrothermal reduction process decreases the spatial dimensions of the sp^2 regions in the graphene, but increases their overall presence in the material. This is possible if the sp^2 sites generated by reduction are isolated from the originally present sp^2 clusters by defects such as vacancies or residual sp^3 carbon. Various

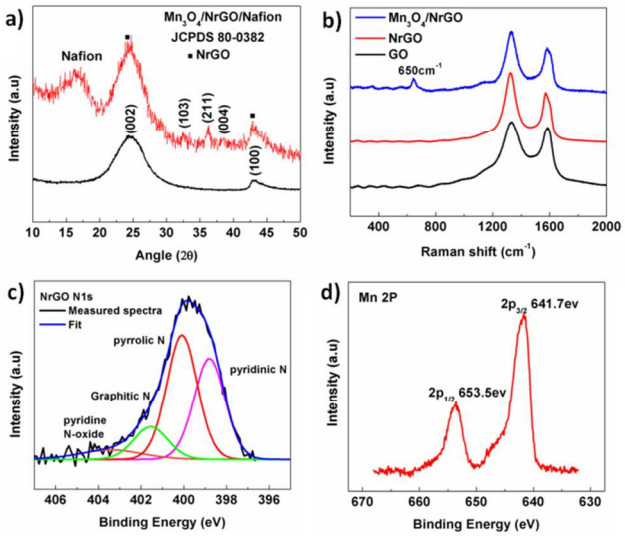

Figure 4. (a) XRD of Mn_3O_4/NrGO and NrGO; (b) Raman spectra of GO, NrGO and Mn_3O_4/NrGO; (c) N 1s XPS spectra of NrGO and (d) Mn 2p XPS of Mn_3O_4/NrGO.

trends in I_D/I_G ratio have been reported in the literature upon reduction of GO. The I_D/I_G ratio has been reported to increase,[39-41] decrease, [42, 43] remain nearly constant,[44, 45] or decrease following an increase.[46] In all cases, an appreciable D-peak signal has been observed, indicating that significant disorder remains in the reduced sample. It should be noted that in our study an additional factor which contributes to the enhancement of the D band intensity upon hydrothermal reduction is the incorporation of N dopants.[47, 48] The Mn_3O_4/NrGO architecture shows an additional peak at 650 cm^{-1}, which is characteristic of the Hausmannite Mn_3O_4 phase, confirming further its presence. It is assigned to the A_{1g} mode, which corresponds to the Mn-O breathing vibration of divalent manganese ions in tetrahedral coordination.[22, 49-51]

X-ray photo emission spectroscopy provided further evidence on the oxidation state of Mn and determined the elemental composition of NrGO. The oxygen and nitrogen contents in the NrGO were estimated as 9.0 at% and 4.1 at% respectively. The carbon to oxygen ratio was 9.6 indicating a moderate level of reduction. The N 1s in NrGO can be divided into four components pyridinic N (398.8 eV), pyrrolic N (400.0 eV) substitutional (401.54 eV) and pyridine N-oxide (403.4 eV) as shown in Figure 4c and these assignments as in agreement with the literature.[36]

As shown in Figure 4d, Mn 2p core level spectrum displays two peaks at binding energies of 653.50 eV and 641.70 eV, corresponding to the Mn $2p_{1/2}$ and Mn $2p_{3/2}$ spin–orbit states of manganese oxide respectively. The spin-energy separation is an acceptable way for determining the oxidation phase of Mn and in this case the observed separation of 11.8 eV is in agreement with the literature values for the Mn_3O_4.[52, 53] The peak separation between Mn $2p_{3/2}$ and the lowest component of O 1s (Figure S2) is 111.8 eV is also consistent with the reported value of Mn-O for the Mn_3O_4.[54, 55]Additionally the Mn 3s (Figure S3) peak separation is 5.5 eV, which is consistent with the reported literature for Mn_3O_4.[5, 9, 54]

The ORR catalytic activity of the Mn_3O_4/NrGO architecture was studied in a conventional three electrode system in both O_2 saturated and Ar saturated 0.1 M KOH electrolyte solution. Figure 5a presents the steady state cyclic voltammograms of NrGO and Mn_3O_4/NrGO deposited on glassy carbon electrodes, referring to Ag/AgCl electrode. For NrGO a featureless voltammogram was obtained in the absence of oxygen. The development of a quasi rectangular shape is indicative of the co-existence of a high surface area and relatively high conductance. .[64,65] When oxygen is introduced a clear oxygen reduction peak is observed at -0.29 V vs Ag/AgCl. Mn_3O_4/NrGO displayed two distinctive peaks in the absence of oxygen; an oxidation peak at -15 mV and a reduction peak at -0.59 V. When oxygen was introduced an additional reduction peak located at -0.29 V was observed due to oxygen reduction. The results indicate that the presence of redox peaks at -15 mV and -0.59 V are due to oxidation and reduction of MnO_x.[32, 56, 57] Remarkably, for the Mn_3O_4/NrGO architecture the onset potential shifted to more positive direction and the

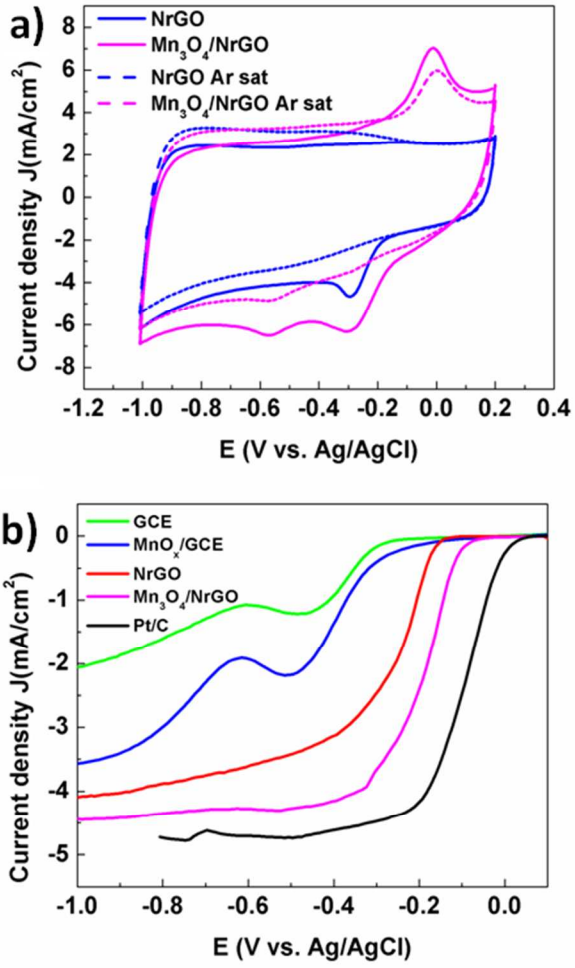

Figure 5. (a) CVs of NrGO and Mn3O4/NrGO in O2 saturated and Ar saturated (b) LSVs of GCE, MnOx/GCE, NrGO, Mn3O4/NrGO and Pt/C at 1600 rpm in O2 saturated 0.1 M KOH solution. LSVs are corrected from blank under Ar. (catalyst loading, NrGO: 0.425 mg/cm^2, Mn3O4/NrGO: 0.45 mg/cm^2 and Pt/C: 0.285 mg/cm^2)

reduction reaction current density was increased compared to the NrGO, indicating that the performance enhancement is brought by the introduction of Mn_3O_4 nanoflakes in the integrated structure.

To gain a better insight on the beneficial role of NrGO as a support for the Mn_3O_4 nanoflakes we investigated the morphology, structure and ORR performance of electrodeposited MnO_x directly on GCE under a sequence of 2, 5, and 10 cycles (CVs) (see support information Figures S4 and S5). There is a progressive growth of MnO_x nanoflakes between 2 and 10 cycles on the GCE, which is getting more dense and uniform at 10 cycles. Overall MnO_x nanoflakes grow at a higher rate on NrGO than on GCE. Raman spectra (Figure S4) from the electrodeposited MnO_x/GCE under 10 cycles show a distinct broad peak centered around 650 cm^{-1}, which is indicative of Mn_3O_4 phase.[22, 49-51] The broadness and low intensity of the peak indicate a high degree of disorder. From the CVs the ORR reduction current at -0.45 V increases with the deposition cycles. Similarly linear sweep voltammograms (LSVs) show an increase in the current at the diffusion controlled limited region, which is related to an increase in active sites due to enhanced surface area.

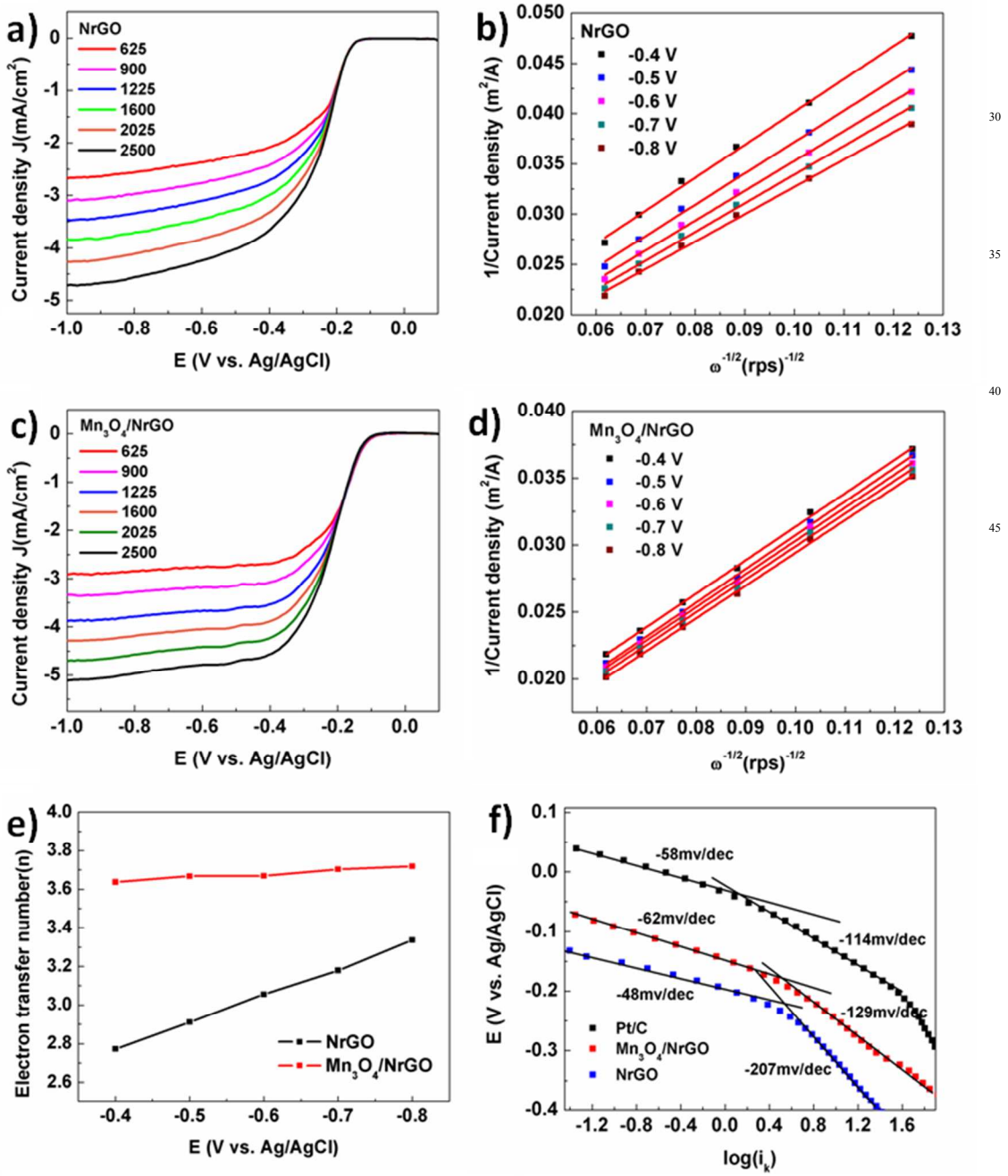

Figure 6. (a) RDE of NrGO at different rotation rates in O_2 saturated 0.1 M KOH (b) K-L plots of NrGO in the voltage range -0.4 V to -0.8 V. (c) RDE of Mn_3O_4/NrGO at different rotation rates in O_2 saturated 0.1 M KOH solution. (d) K-L plots Mn_3O_4/NrGO in the voltage range -0.4 V to -0.8 V. (e) Electron transfer numbers of NrGO, Mn_3O_4/NrGO and Pt/C. (f) Tafel plots of Mn_3O_4/NrGO and Pt/C.

However the onset potential does not move appreciably.

Rotating disk electrode analysis of Mn_3O_4/NrGO catalyst together with that of NrGO, MnO_x and bare GCE and state of the art commercial Pt/C catalyst (20 wt% Pt on Vulcan XC-72) is presented in Figure 5. The half wave potentials of NrGO, Mn_3O_4/NrGO are located at -0.26 V and -0.2 V respectively, confirming that Mn_3O_4/NrGO has better electrocatalytic activity towards oxygen reduction reaction than NrGO. The Mn_3O_4/NrGO displays a limiting current density of 4.4 mA/cm^2 at -0.4 V, which is higher than that of NrGO (3.2 mA/cm^2) and comparable with that on Pt/C (4.7 mA/cm^2).

To evaluate the electron transfer numbers linear sweeps were measured at different rotation rates for NrGO and Mn_3O_4/NrGO as shown in Figure 6a and 6c.The transferred electrons were calculated by the Koutecky-Levich (K-L) equation (1) and the K-L plots for NrGO and Mn_3O_4/NrGO are shown in Figure 6b and 6d. The electron transfer numbers for NrGO vary between 2.7 to 3.3 throughout the voltage range of -0.4 V to -0.8 V. In Figure 6c which presents LSVs for Mn_3O_4/NrGO at different rotating speeds, three separate potential regions can be observed. At low

potentials E < -0.2 V, the ORR is under kinetic control. The potential range -0.2 V to -0.4 V is mixed kinetic-diffusion region. At high potentials (E > -0.4 V), the ORR is controlled by O_2 diffusion. In Figure 6d, good linear fitting can be seen for each potential with identical slope and the calculated electron transfer numbers at the Mn_3O_4/NrGO electrode are close to 3.7. The ORR performance of the Mn_3O_4/NrGO deposited on carbon fiber paper deteriorated upon annealing at low temperatures up to 300 ^oC (Figure S11, S12) and no improvement in the crystallinity Mn_3O_4 phase was observed (Figure S13)

It is well known that in alkaline electrolytes, oxygen may be reduced through a direct four electron reduction process to OH^- following reaction (2), or through a series (2e X 2e) pathway involving a peroxide HO_2^- intermediate, via reactions (3) and (4). Alternatively, the HO_2^- formed in reaction (3) may disproportionate to OH^- and O_2 according to reaction (5). Reactions (4) and (5) may proceed concurrently so that the O_2 formed in (5) is subsequently reduced back to peroxide through reaction (3) with equations (4) and (5) cycled repeatedly until all the O_2 is converted to OH^-. If reactions (4) and (5) are very fast, it would then appear as if oxygen is reduced directly to OH^- through the four electron transfer process.

$$O_2 + 2H_2O + 4e \longrightarrow 4OH^- \quad (2)$$

$$O_2 + H_2O + 2e \longrightarrow HO_2^- + OH^- \quad (3)$$

$$HO_2^- + H_2O + 2e \rightarrow 3OH^- \quad (4)$$

$$HO_2^- \rightarrow \frac{1}{2}O_2 + OH^- \quad (5)$$

In an effort to understand the ORR process occurring on Mn_3O_4/NrGO, the H_2O_2 reduction reaction (HORR) and oxygen reduction reaction ORR was measured over Mn_3O_4/NrGO, NrGO and MnO_x electrodes as shown in Figure S7. An H_2O_2 concentration of 1.3 mM was used, which is same as O_2 concentration in O_2 saturated 0.1 M KOH solution**.** The HORR current on MnO_x is rather significant when compared to the ORR current in higher voltage region, which indicates that the MnO_x is active for both ORR and HORR when electrodeposited on GC electrode. In the case of both NrGO and Mn_3O_4/NrGO the HORR current is far less than the ORR current. This indicates that both NrGO and Mn_3O_4/NrGO are rather inactive towards the HORR.[58, 59] These observations suggest that the likely mechanism on the Mn_3O_4/NrGO for overall 4e ORR takes place by series pathway via peroxide disproportionation reaction as exemplified by equations 3 and 5. First a two-electron reduction to hydrogen peroxide at low overpotential occurs at NrGO (low n numbers) and subsequently Mn_3O_4 catalyzes the disproportionation of HO_2^- intermediates. Several groups have also proposed that reactions 3 and 5 are the likely mechanism to takes place on MnO_x/carbon catalysts.[14, 28, 29, 32, 60] The morphology of the integrated Mn_3O_4/NrGO electrode could also play a critical role in producing the exceptional catalytic activity by the suggested disproportionation intermediate mechanism. For example, the porous structure of the electrode may trap peroxide intermediates and thus facilitate the disproportionation pathway. Figure 6f presents the mass-corrected Tafel plots of the logarithm of kinetic current density, log I_k (mA cm^{-2}), vs. the electrode potential E for the ORR on the NrGO, Mn_3O_4/NrGO and Pt/C electrodes in an O_2 saturated 0.1 M KOH solution. Kinetic current densities were extracted from the steady-state polarization according to the Koutecky−Levich equation.

$$J_k = \frac{J_D * J}{(J - J_D)} \quad (6)$$

where J_D is the diffusion-limiting current density. These Tafel curves were derived from the polarization curves of Figure 5b with a rotation rate of 1600 rpm. Two distinct Tafel slopes at low and high potential regions are observed for each catalyst, which indicate that oxygen reduction occurred by different mechanisms in these two regions. At low overpotentials, the Tafel slopes for NrGO, Mn_3O_4/NrGO and Pt/C are -48, -62 and -58 mV dec^{-1}, while at high overpotentials the corresponding slopes are -207, -129 and -114 mV dec^{-1}. The two different Tafel slopes for each catalyst result from different adsorbed oxygen coverage, which follows a Temkin isotherm (high coverage) at low overpotentials and a Langmuir isotherm (low coverage) at higher overpotentials.[60] Theoretically, a Tafel slope of -60 mV dec^{-1} at low overpotentials is associated with an intermediate oxide coverage arising from ORR, whereby the first electron transfer step involving an adsorbed product is the rate-determining step (Temkin isotherm). On the other hand a Tafel slope of -120 mV dec^{-1} at high overpotentials can be explained by a migration of adsorbed oxygen intermediates, which is commonly the case when a two-electron transfer reaction is the rate-determining step (Langmuir isotherm).[61] The Tafel slopes of Mn_3O_4/NrGO in low and high potential regions are very close to the values of Pt/C catalyst. This demonstrates that the oxygen adsorption mechanism of Mn_3O_4/NrGO is similar to that of Pt/C catalyst. For NrGO, the Tafel slope values of -48 mV dec^{-1} and -207 mV dec^{-1} in low and high current density regions were significantly different and accounts for the lower activity of the NrGO catalysts. Detailed comparisons of the ORR activity of our Mn_3O_4/NrGO catalyst with other representative manganese oxide catalysts[9,16-27,31] are presented in Table S2.The Mn_3O_4/NrGO is among the most active MnO_x based catalysts in terms of half wave potential and limiting current density.

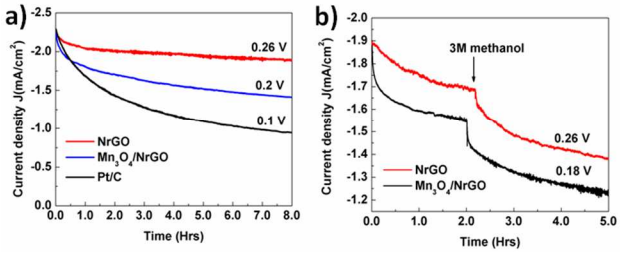

Figure 7. (a) Chronoamperometric responses of NrGO, Mn_3O_4/NrGO and Pt/C. (b) Methanol poisoning of NrGO, Mn_3O_4/NrGO.

Other important performance metrics for an ORR catalyst include cyclic stability and tolerance to fuel molecules such as methanol, which is of importance to direct methanol fuel cells. The stability of NrGO, Mn_3O_4/NrGO and Pt/C were evaluated by monitoring the chronoamperometric response at the half wave potential of each electrode rotated at 1600 rpm in oxygen saturated 0.1 M KOH solution. As shown in Figure 7a, the Mn_3O_4/NrGO showed

a higher stability than the Pt/C, retaining 63% of its initial current after 8hrs of testing. The smallest attenuation in the catalytic activity for all three electrodes was observed for the NrGO, which lost only 15% of its initial activity. The electrodes were further tested for possible crossover in the presence of 3M methanol at 0.26 V and 0.18 V for NrGO and Mn_3O_4/NrGO Figure 7b. After the addition of methanol the ORR current for NrGO and Mn_3O_4/NrGO decreased by 4.2% and 6.5% respectively, while that for Pt/C suffered a major shift from cathodic to anodic as a result of methanol oxidation reaction (see supporting information Figure S10). The results indicate that both Mn_3O_4/NrGO and NrGO have excellent immunity towards methanol cross over which overcomes a main challenge faced by precious metal catalysts in fuel cells.

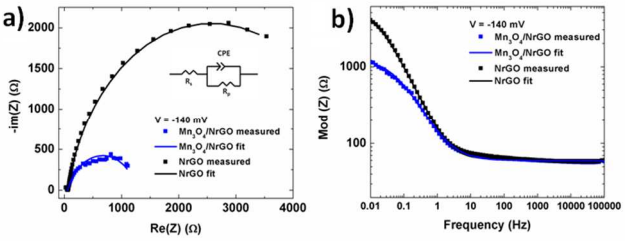

Figure 8. (a) Nyquists plots and (b) Bode plots of NrGO and Mn3O4/NrGO obtained by applying a potential of – 140 mV, over the frequency range from 100 kHz to 10 mHz.

Electrochemical impedance spectroscopy (EIS) is a useful technique to characterize interface reactions and electrode kinetics in ORR. Figure 8 shows representative Nyquist plots of the EIS response of Mn_3O_4/NrGO and NrGO electrodes at overpotential of -140 mV where ORR is taking place. The data were fit using the equivalent circuit illustrated in the inset of Figure 8, and the resultant fitting parameters are summarized in Table S1 (Supporting Information). The Mn_3O_4/NrGO exhibits a smaller semicircle when compared to NrGO, which clearly demonstrates that the Mn_3O_4/NrGO electrode possess a lower charge transfer resistance and thus allows a much faster shuttling of electrons during ORR. The results further reflect the electrocatalytic activity of both electrodes for ORR.

Conclusions

In conclusion, 3D hierarchical structure of Mn_3O_4 nanoflakes supported on nitrogenated reduced graphene oxide, exhibiting high performance for the ORR in alkaline medium, was successfully prepared by room temperature electrodeposition. The oxygen reduction of the integrated catalyst followed the apparent four-electron transfer pathway. The oxygen reduction of the integrated catalyst followed the apparent four-electron transfer pathway due to the synergetic effects between Mn3O4 nanoflakes and NrGO. The high surface area network and moderate long range crystalline order of Mn_3O_4 nanoflakes provided ample defects sites for oxygen adsorption, whereas the immediate coupling between the Mn_3O_4 nanoflakes and the conductive NrGO guaranteed efficient electron transport. In addition to high ORR activity, the as prepared Mn_3O_4/NrGO catalyst shows superior methanol tolerance and stability when compared to commercial Pt/C for ORR. Thus Mn_3O_4/NrGO represents a low cost and highly active catalyst which can be used as a cathode in fuel cells or metal-air batteries in alkaline solutions.

Acknowledgements

This work was financially supported by VCRS studentship from the University of Ulster. WZ thanks EPSRC (EP/F019580/1) for financial support on TEM facility. XPS was performed at the National EPSRC XPS User's Service (NEXUS) at Newcastle University, an EPSRC Mid-Range Facility.

Notes and references

[1]*School of Engineering, Engineering Research Institute, University of Ulster, Newtownabbey, BT37 0QB, UK.*
[2]*School of Chemistry, University of St Andrews, St Andrews, KY16 9ST, Scotland, UK.*
[3]*School of the Built Environment, Built Environment Research Institute, University of Ulster, Newtownabbey, BT37 0QB, UK.*
[4]*School of Mechanical and Systems Engineering, University of Newcastle, Stephenson Building, Newcastle upon Tyne NE1 7RU, UK.*
*Corresponding author: p.papakonstantinou@ulster.ac.uk

† Electronic Supplementary Information (ESI) available: [details of any supplementary information available should be included here]. See DOI: 10.1039/b000000x/

‡ Footnotes should appear here. These might include comments relevant to but not central to the matter under discussion, limited experimental and spectral data, and crystallographic data.

1 Y. Liang, Y. Li, H. Wang and H. Dai, *J. Am. Chem. Soc.,* 2013, **135,** 2013.
2 F. Cheng and J. Chen, *Chem. Soc. Rev.,* 2012, **41,** 2172.
3 W. Xiao, D. Wang and X. W. Lou, *J. Phys. Chem. C,* 2010, **114,** 1694.
4 Y. Liang, H. Wang, P. Diao, W. Chang, G. Hong, Y. Li, M. Gong, L. Xie, J. Zhou, J. Wang, T. Z. Regier, F. Wei and H. Dai, *J. Am. Chem. Soc.,* 2012, **134,** 15849.
5 K. L. Pickrahn, S. W. Park, Y. Gorlin, H. Lee, T. F. Jaramillo and S. F. Bent, *Advanced Energy Materials,* 2012, **2,** 1269.
6 F. Cheng, T. Zhang, Y. Zhang, J. Du, X. Han and J. Chen, *Angewandte Chemie International Edition,* 2013, **52,** 2474.
7 Q. Tang, L. Jiang, J. Liu, S. Wang and G. Sun, *ACS Catalysis,* 2014, **4,** 457.
8 S. R. N. Hamdani.M Chartier.P, *Int. J. Electrochem. Sci.,* 2010, **5,** 556.
9 Y. Gorlin, C. Chung, D. Nordlund, B. M. Clemens and T. F. Jaramillo, *ACS Catal.,* 2012, **2,** 2687.
10 Y. Liang, Y. Li, H. Wang, J. Zhou, J. Wang, T. Regier and H. Dai, *Nat Mater,* 2011, **10,** 780.
11 Z. Wu, S. Yang, Y. Sun, K. Parvez, X. Feng and K. Müllen, *J. Am. Chem. Soc.,* 2012, **134,** 9082.
12 J. Suntivich, H. A. Gasteiger, N. Yabuuchi, H. Nakanishi, J. B. Goodenough and Y. Shao-Horn, *Nat Chem,* 2011, **3,** 546.
13 K. A. Stoerzinger, M. Risch, J. Suntivich, W. M. Lu, J. Zhou, M. D. Biegalski, H. M. Christen, Ariando, T. Venkatesan and Y. Shao-Horn, *Energy Environ. Sci.,* 2013, **6,** 1582.
14 T. Poux, F. S. Napolskiy, T. Dintzer, G. Kéranguéven, S. Y. Istomin, G. A. Tsirlina, E. V. Antipov and E. R. Savinova, *Catalysis Today,* 2012, **189,** 83.
15 E. Fabbri, R. Mohamed, P. Levecque, O. Conrad, R. Kötz and T. J. Schmidt, *ACS Catalysis,* 2014, **4**, 1061
16 J. Lee, T. Lee, H. Song, J. Cho and B. Kim, *Energy Environ. Sci.,* 2011, **4,** 4148.
17 J. Lee, G. S. Park, H. I. Lee, S. T. Kim, R. Cao, M. Liu and J. Cho, *Nano Lett.,* 2011, **11,** 5362.
18 J. Feng, Y. Liang, H. Wang, Y. Li, B. Zhang, J. Zhou, J. Wang, T. Regier and H. Dai, *Nano Research,* 2012,**5**,718.

19 Y. Tan, C. Xu, G. Chen, X. Fang, N. Zheng and Q. Xie, *Advanced Functional Materials,* 2012,**22,** 4584.
20 J. Zhang, C. Guo, L. Zhang and C. M. Li, *Chem. Commun.,* 2013, **49,** 6334.
21 F. Cheng, J. Shen, W. Ji, Z. Tao and J. Chen, *ACS Appl. Mater. Interfaces,* 2009, **1,** 460.
22 J. Duan, S. Chen, S. Dai and S. Z. Qiao, *Advanced Functional Materials,* 2013, **(**doi: 10.1002/adfm.201302940).
23 S. Bag, K. Roy, C. S. Gopinath and C. R. Raj, *ACS Applied Materials & Interfaces,* 2014, **6**, 2692.
24 T. N. Lambert, D. J. Davis, W. Lu, S. J. Limmer, P. G. Kotula, A. Thuli, M. Hungate, G. Ruan, Z. Jin and J. M. Tour, *Chem. Commun.,* 2012, **48,** 7931.
25 J. Duan, Y. Zheng, S. Chen, Y. Tang, M. Jaroniec and S. Qiao, *Chem.Commun.,* 2013, **49,** 7705.
26 K. Jung, J. Lee, S. Yoon, S. Yeon, W. Chang, K. Shin and J. Lee, *J. Mater. Chem.,* 2012, **22,** 21845.
27 W. Sun, A. Hsu and R. Chen, *J. Power Sources,* 2011, **196,** 627.
28 L. Mao, D. Zhang, T. Sotomura, K. Nakatsu, N. Koshiba and T. Ohsaka, *Electrochim. Acta,* 2003, **48,** 1015.
29 F. Cheng, Y. Su, J. Liang, Z. Tao and J. Chen, *Chem. Mater.,* 2010, **22,** 898.
30 F. Hu, X. Zhang, F. Xiao and J. Zhang, *Carbon,* 2005, **43,** 2931.
31 Y. Gorlin and T. F. Jaramillo, *J. Am. Chem. Soc.,* 2010, **132,** 13612.
32 F. H. B. Lima, M. L. Calegaro and E. A. Ticianelli, *Electrochim. Acta,* 2007, **52,** 3732.
33 L. Zhang and Z. Xia, *The Journal of Physical Chemistry C,* 2011, **115,** 11170.
34 L. Zhang, J. Niu, L. Dai and Z. Xia, *Langmuir,* 2012, **28,** 7542.
35 C. Zhu, S. Guo, Y. Fang, L. Han, E. Wang and S. Dong, *Nano Research,* 2011, **4,** 648.
36 D. Long, W. Li, L. Ling, J. Miyawaki, I. Mochida and S. Yoon, *Langmuir,* 2010, **26,** 16096.
37 G. Eda and M. Chhowalla, *Adv Mater,* 2010, **22,** 2392.
38 D. R. Dreyer, S. Park, C. W. Bielawski and R. S. Ruoff, *Chem. Soc. Rev.,* 2010, **39,** 228.
39 S. Stankovich, D. A. Dikin, R. D. Piner, K. A. Kohlhaas, A. Kleinhammes, Y. Jia, Y. Wu, S. T. Nguyen and R. S. Ruoff, *Carbon,* 2007, **45,** 1558.
40 V. C. Tung, M. J. Allen, Y. Yang and R. B. Kaner, *Nat Nano,* 2009, **4,** 25.
41 J. I. Paredes, S. Villar-Rodil, P. Solís-Fernández, A. Martínez-Alonso and J. M. D. Tascó, *Langmuir,* 2009, **25,** 5957.
42 N. Mohanty, A. Nagaraja, J. Armesto and V. Berry, *Small,* 2010, **6,** 226.
43 V. Lee, L. Whittaker, C. Jaye, K. M. Baroudi, D. A. Fischer and S. Banerjee, *Chemistry of Materials,* 2009, **21,** 3905.
44 C. Mattevi, G. Eda, S. Agnoli, S. Miller, K. A. Mkhoyan, O. Celik, D. Mastrogiovanni, G. Granozzi, E. Garfunkel and M. Chhowalla, *Advanced Functional Materials,* 2009, **19,** 2577.
45 C. Gómez-Navarro, R. T. Weitz, A. M. Bittner, M. Scolari, A. Mews, M. Burghard and K. Kern, *Nano Letters,* 2007, **7,** 3499.
46 H. Wang, J. T. Robinson, X. Li and H. Dai, *J. Am. Chem. Soc.,* 2009, **131,** 9910.
47 T. Szabó, O. Berkesi, P. Forgó, K. Josepovits, Y. Sanakis, D. Petridis and I. Dékány, *Chemistry of Materials,* 2006, **18,** 2740.
48 D. Geng, S. Yang, Y. Zhang, J. Yang, J. Liu, R. Li, T. Sham, X. Sun, S. Ye and S. Knights, *Appl. Surf. Sci.,* 2011, **257,** 9193.
49 C. M. Julien, M. Massot and C. Poinsignon, *Spectrochimica Acta Part A: Molecular and Biomolecular Spectroscopy,* 2004, **60,** 689.
50 P. Si, X. Dong, P. Chen and D. Kim, *J. Mater. Chem. B,* 2013, **1,** 110.
51 L. Li, K. H. Seng, H. Liu, I. P. Nevirkovets and Z. Guo, *Electrochim. Acta,* 2013, **87,** 801.
52 D. P. Dubal, D. S. Dhawale, R. R. Salunkhe and C. D. Lokhande, *J Electroanal Chem,* 2010, **647,** 60.
53 A. Moses Ezhil Raj, S. G. Victoria, V. B. Jothy, C. Ravidhas, J. Wollschläger, M. Suendorf, M. Neumann, M. Jayachandran and C. Sanjeeviraja, *Appl. Surf. Sci.,* 2010, **256,** 2920.
54 M. Toupin, T. Brousse and D. Bélanger, *Chem. Mater.,* 2002, **14,** 3946.
55 M. Chigane and M. Ishikawa, *Journal of the Electrochemical Society,* 2000, **147,** 2246.
56 R. B. Valim, M. C. Santos, M. R. V. Lanza, S. A. S. Machado, F. H. B. Lima and M. L. Calegaro, *Electrochim. Acta,* 2012, **85,** 423.
57 L. Wei, C. Li, H. Chu and Y. Li, *Dalton Trans.,* 2011, **40,** 2332.
58 J. Liu, L. Jiang, Q. Tang, B. Zhang, D. S. Su, S. Wang and G. Sun, *ChemSusChem,* 2012, **5,** 2315.
59 F. Jaouen and J. Dodelet, *The Journal of Physical Chemistry C,* 2009, **113,** 15422.
60 F. H. B. Lima, M. L. Calegaro and E. A. Ticianelli, *J Electroanal Chem,* 2006, **590,** 152.
61 N. M. Marković, T. J. Schmidt, V. Stamenković and P. N. Ross, *Fuel Cells,* 2001, **1,** 105.
62 G. Eda, G. Fanchini and M. Chhowalla, *Nat Nano,* 2008, **3,** 270.
63 A. Ganguly, S. Sharma, P. Papakonstantinou and J. Hamilton, *J. Phys. Chem. C,* 2011, **115,** 17009.
64 L. Qu, Y. Liu, J.-B. Baek, L. Dai, *ACS Nano***,** 2010, **4,** 1321.
65 Y. Li, Z. Huang, K. Huang, D. Carnahan, Y. Xing, *Energy & Environmental Science,* 2013, **6,** 3339.